Physical Review E (accepted 25 June 2018)

On estimating stable and unstable sets and their role as transport barriers in stochastic flows

Sanjeeva Balasuriya
School of Mathematical Sciences, University of Adelaide, Adelaide SA 5005, Australia *

Georg A. Gottwald
School of Mathematics and Statistics, University of Sydney, Sydney NSW 2006, Australia †
(Dated: June 28, 2018)

We consider the situation of a large-scale stationary flow subjected to small-scale fluctuations. Assuming that the stable and unstable manifolds of the large-scale flow are known, we quantify the mean behaviour and stochastic fluctuations of particles close to the unperturbed stable and unstable manifolds and their evolution in time. The mean defines a smooth curve in physical space, while the variance provides a time- and space-dependent quantitative estimate where particles are likely to be found. This allows us to quantify transport properties such as the expected volume of mixing as the result of the stochastic fluctuations of the transport barriers. We corroborate our analytical findings with numerical simulations in both compressible and incompressible flow situations. We moreover demonstrate the intimate connection of our results with finite-time Lyapunov exponent fields, and with spatial mixing regions.

PACS numbers: 05.45.-a, 05.40.Jc, 47.51.+a, 47.10.Fg
Keywords: Invariant manifolds; Lagrangian coherent structures; stochastic differential equations; fluid mixing; uncertainty in flow barriers

I. INTRODUCTION

Lagrangian coherent structures [1–3] have a well-established importance in fluid flows. Loosely speaking, they consist of fluid regions which move 'almost' coherently, and their boundaries act as transport barriers separating the inside of the structure from the outside, at least for some time. The boundaries of Lagrangian structures are analogues of stable and/or unstable manifolds. In applications these boundaries are identified using a variety of different techniques which take into account that data is usually only known for finite times [4, 5]. The analysis of these time-varying boundaries (which, confusingly, are themselves sometimes referred to as Lagrangian coherent structures) between coherent fluid blobs has seen many recent applications, ranging from geophysical [6] to microfluidic [7] scales. Environmental applications include oil spills [8], garbage in the ocean [9], coral protection [10], plankton distribution [11], ozone depletion [12], transport of biological spores [13] and atmospheric wind hazards near airports [14]. Additional applications include determining a 'skeleton for turbulence' [2, 15], microfluidic mixing optimisation [7] and fisheries [6]. In essentially all these applications, the velocity field is considered *deterministic*.

Most realistic flow situations are, however, typically of a *stochastic* nature, related to the uncertainties present in any data, model, or simulation [16–19]. The stochasticity naturally enters coarse-grained macroscopic degrees of freedom, that is, those which we observe, in a multiscale setting. Recent work has extended the classical deterministic framework of Eulerian partial differential equations for fluid flows to stochastic partial differential equations [20–25] where the stochasticity enters on the side of the Lagrangian particle dynamics. The stochasticity arises as the integrated effect of the fast small-scale degrees of freedom by the process of homogenisation [25–28], and describes the effect of the unresolved fast processes onto the resolved slow degrees of freedom. Thus, there is a need to incorporate the effect of stochasticity into the deterministic approaches for understanding and quantifying transport between coherent structures. The natural extension from deterministic intuition may be to think of stable and unstable manifolds of the *stochastic* system to demarcate transport barriers. While there exists deep theory for defining stable and unstable manifolds in stochastic differential equations (usually falling under 'random dynamical systems' approaches) [29–38], there is at present little insight on how such theory can be adapted to quantify transport barriers, and/or determine mixing across these.

In this paper, we restrict to two-dimensional flows, motivated by the fact that oceanic flows are weakly two-dimensional in that there is dominant flow on two-dimensional isopycnal surfaces [39]. Since these surfaces are not necessarily uniformly spaced, three-dimensional incompressibility does *not* translate to two-dimensional divergence-free velocity fields on each surface, and therefore we allow for general compressibility in our work. We

* sanjeevabalasuriya@yahoo.com
† georg.gottwald@sydney.edu.au

consider the following idealized situation: We assume that there is a large-scale flow which is slowly varying in time and which can be viewed as steady for some characteristic time scale τ_c. The large-scale flow is subjected to small-scale disturbances which we model as a stochastic forcing of the large-scale flow, along the lines described above. Let us assume that we have knowledge of the stable and/or unstable manifold of the deterministic large-scale flow from some coarse-grained measurements at some time t_1. Our aim here is to describe the effect of the stochasticity on the temporal evolution of these manifolds. More specifically: extending the notion of stable and unstable manifolds in this setting, and quantifying transport and mixing properties and their uncertainty.

The presence of stochasticity destroys the natural notions of stable and unstable manifolds, necessitating a definition of what a backward-time or forward-time flow barrier is. Following a recently developed idea for general curves in two-dimensional flows [40], our approach here is to study the statistics of the initial-time flow barrier over many realisations of the noise. For each realisation we define *stable/unstable sets* which are determined by flowing in time the initially known locations of the stable and unstable manifolds. Depending on an interpretation of how the driving noise is implemented, these sets can take different forms. If the same noise realisation is used across all initial conditions, we are in the classical domain of random dynamical systems, in which the stable/unstable sets are indeed smooth curves for each realisation, and therefore can be termed (random) stable/unstable manifolds [29–38]. On the other hand, we introduce in this paper an alternative scenario, in which the noise realisations are nonuniform across initial positions. This corresponds to the viewpoint that each fluid particle is subject to a different noise realisation. The stable/unstable sets in this case will consist of an uncountable collection of points which do not form a curve. The statistical behaviour of the stable/unstable sets in either case is characterised by their *mean*—a smooth curve in space—and their *variance*. The former identifies the average location of particles, while the latter quantifies the width or uncertainty of the mean behaviour. It is this uncertainty quantification of transport barriers—albeit in a simplified setting—that forms the main contribution of this article.

We remark that uncertainty quantification of propagating structures typically has two aspects: the uncertainty in the identification at the initial time, and the uncertainty engendered through propagation by uncertain velocities. We address here the latter aspect, assuming that the stable and unstable manifolds are known at some initial time. In identifying transport barriers (i.e., analogues of stable/unstable manifolds) over a finite-time duration, we note that this is nonunique even in *deterministic* flows [41]. This has led to the preponderance of different methods, often called 'Lagrangian coherent structure' (LCS) methods, which continue to be developed to identify these (for reviews, see [1, 3, 41, 42]). These methods include ridges of finite-time Lyapunov exponents (FTLEs) [1, 43–50], curves/surfaces towards which there is extremal repulsion/attraction [1, 51–56], sets which are 'almost coherent' with respect to the operation of a transfer operator [57–61], identification of vorticity cores or oscillations [62, 63], etc. Thus, the very definition of 'transport barrier' at some finite time is ambiguous. If following finite-time Lyapunov exponent ideas, for example, one is seeking the infinite-time property of stable/unstable manifolds as initial conditions which decay exponentially in forward/backward times; however, in finite-time situations, *any* continuous function f of time t in a finite-time interval can be bounded in the form $|f(t)| \leq Ae^{\lambda t}$, where λ is any given positive constant, by choosing A appropriately. Thus, exponential stretching is no more than a *diagnostic* for determining (an analogue of) a stable/unstable manifold; using ridges of finite-time Lyapunov exponents does not constitute a watertight way of defining stable/unstable manifolds [50, 51]. On the other hand, it has come to be expected that some types of transport barriers in finite-time flows (those which are analogous to stable/unstable manifolds) carry an exponential stretching signature. We verify this property in the first example that we consider—an incompressible flow in Section III—in validating our uncertainty theory for transport barriers under stochastic perturbations.

An advantage of our approach is that it enables a spatial quantification of the *mixing* imparted by the stochasticity, complementing the notion of partitioning space into regions which are dominantly coherent under noise [58, 59, 64, 65]. The fluctuations around the mean curve leads to the potential for transport between regions which, in the absence of stochasticity, would be identified as separate physical regions. We argue that the variance (with respect to realisations of the noise) describes the leakiness between the regions separated by the mean curves. The leakiness is an averaged mean quantity and does not describe the behaviour of a single particle but rather of an ensemble of particles. From a practical perspective, the crucial insight is that, under the assumption of ergodicity of the stochastic dynamical system, the variance is related to the relative volume of mass of an initial distribution of particles that will be leaking at a specified finite time. This quantity is important, for example, when estimating the spatial distribution of oil spills and knowledge of the time-dependent spatially varying variance around the mean curve can be used to assess the extent of further oil contamination. Our second example, focussing on Taylor-Green flow in Section IV, validates that our theory correctly identifies *mixing regions* and their evolution with time.

The paper is organised as follows. In Section II we present the theory for the time-evolution of stochastically perturbed stable and unstable manifolds. This provides explicit analytical formulæ for the mean of the stable and unstable sets as well as their variances. We show that the

variance—as a measure of uncertainty—saturates under generic conditions. Section III applies the theory to an example of a compressible flow and presents numerical simulations illustrating the ability of our framework to capture the statistics of Lagrangian particle dynamics near stochastically perturbed stable and unstable manifolds. Moreover, we show that our analytical framework identifies structures which are aligned with FTLE ridges, with the ridge thickness variation being predicted by our theoretical variance. Section IV then treats an incompressible flow example, and shows how the ideas of transport barriers developed in the deterministic situation can be extended to the stochastic case. We show that the interchange of fluids across the transport barrier is spatially correlated to the variance of the stable/unstable sets. We conclude in Section V with a discussion and an outlook.

II. MANIFOLD UNCERTAINTY

A. Stable/unstable sets

Let $x \in \Omega$, where Ω is a two-dimensional connected open set. Let $v : \Omega \to \mathbb{R}^2$ be (sufficiently) smooth, and consider the deterministic dynamical system

$$\dot{x} = v\,(x)\ . \tag{1}$$

If v is a velocity field of a fluid, then solutions to (1) are flow trajectories. We restrict here to a slowly varying large scale flow which can be considered as steady for times smaller than some characteristic time scale τ_c. For such flows, (1) can be considered the leading-order approximation. Suppose (1) possesses a hyperbolic fixed point a to which is attached a one-dimensional stable manifold Γ^s and a one-dimensional unstable manifold [66] Γ^u. These are shown by the thick curves in Fig. 1, and are respectively parametrised by $x^s(t)$ and $x^u(t)$, both solutions of (1). In deterministic systems (1) manifolds of this sort are specifically important since they are *flow separators* (flow barriers, transport barriers) in terms of particle trajectories. Consider for example a blob of fluid placed on top of the stable manifold Γ^s as shown in Fig. 1. As this blob evolves according to (1), it eventually gets close to a. At this point, it is strongly influenced by the unstable manifold Γ^u, and the blob gets stretched (exponentially fast) along Γ^u. Thus, particles in the blob which were on one side of Γ^s get stretched in one direction, while those on the other side of the blob are stretched in the other direction. In this sense, Γ^s is a flow separator in forward-time. Similarly, Γ^u is a flow separator in backward-time. We remark that these interpretations continue to hold when v is *unsteady*; in this instance a is not a fixed point, but a time-varying trajectory to which is attached stable/unstable manifolds. The flow-barrier property is well-known, and is a fundamental reason why finite-time analogues of stable and unstable manifolds (e.g., strong ridges of finite-time Lyapunov exponent fields [3], curves to which there is maximal attraction [1], etc) are investigated numerically as flow barriers in realistic flows.

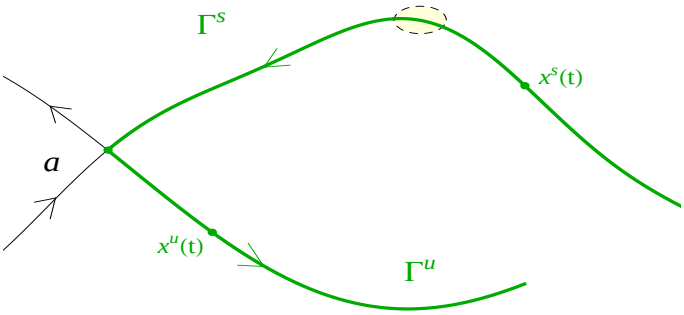

FIG. 1. Stable (Γ^s) and unstable (Γ^u) manifolds of the fixed point a of (1).

We want to determine the intuitive counterparts to these—i.e., intuitive flow barriers—when the coarse-grained large-scale flow (1) is subjected to small-scale fluctuation. We model the resulting flow by a stochastically perturbed version of (1). We assume that the unstable/stable manifold is known at some time t_1, and aim to determine its subsequent evolution and uncertainty up to some time t which is smaller than the characteristic time scale of the large-scale flow τ_c. We will discuss this under two slightly different interpretations of the perturbing stochastic differential equation (SDE).

We first consider the Itô stochastic differential equation (SDE)

$$\mathrm{d}y = v\,(y)\ \mathrm{d}t + \varepsilon\,\sigma\,(y,t)\,\mathrm{d}W_t, \tag{2}$$

for $y \in \Omega$ for initial condition $y(t_1) = \zeta$. Here, ε is a dimensionless parameter representing the size ($|\varepsilon| \ll 1$) of the stochasticity, $\mathrm{d}W_t$ is two-dimensional Brownian motion, and σ is a 2×2 matrix with components σ_{ij}—in general both spatially and temporally dependent—incorporating anisotropic diffusion. In the form (2) above, the first term is the 'drift' and the second the 'diffusion' associated with the variable y. The SDE (2), if interpreted as the Lagrangian description of fluid parcels assumes the same realisation of noise W_t for all fluid particles. This model is what is usually studied in the framework of slow manifolds in random dynamical systems, which establishes the existence of smooth manifolds for each noise realisation [29–38]. The manifolds can be initialised at time t_1 by choosing a collection of initial conditions for the ζ. The time t, until which we plan to describe the manifold evolution can be any value such that $|t - t_1| \ll \tau_c$, the characteristic time scale of the large-scale flow, to assure steadiness of the manifolds $\Gamma^{u,s}$. The unstable manifold is propagated forward in time with $t > t_1$ whereas the stable manifold is propagated backward in time with $t < t_1$.

We also consider a slightly different viewpoint in which *each initial condition is allowed to be driven by indepen-*

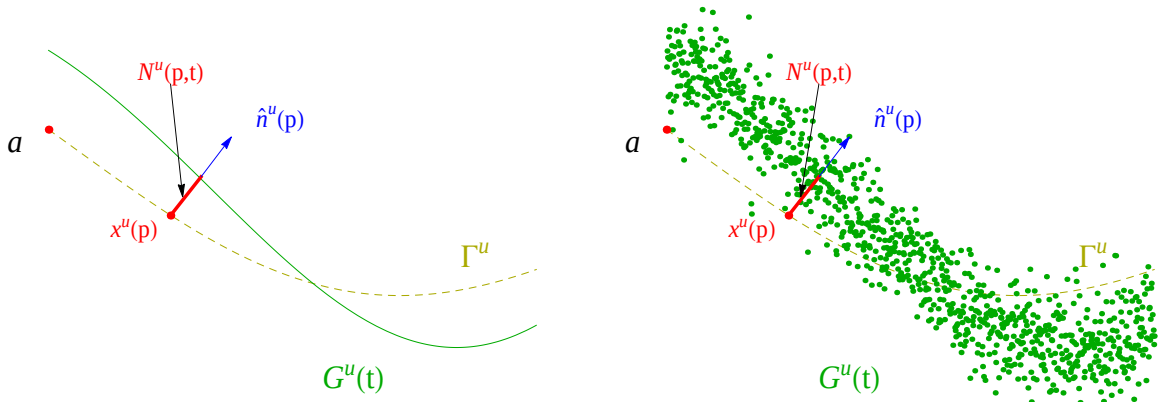

FIG. 2. Illustration of the geometry of the finite-time random unstable set $G^u(t)$ (green) in a time-slice t and the deterministic unstable manifold Γ^u (dashed yellow). Left: For the SDE (2) with uniform noise $G^u(t)$ is a smooth curve. Right: For the SDE (3) with nonuniform noise $G^u(t)$ is an uncountable collection of random points.

dent noise realisations. In particular, we consider

$$\mathrm{d}y^{(\zeta)} = v\left(y^{(\zeta)}\right)\,\mathrm{d}t + \varepsilon\,\sigma\left(y^{(\zeta)},t\right)\mathrm{d}W_t^{(\zeta)}, \qquad (3)$$

where $y^{(\zeta)}$ denotes conditioning on the initial value $y(t_1)=\zeta$, and the noise realisation are independent with $\mathbb{E}[W_t^{(\zeta)}W_s^{(\xi)}] = \delta(\zeta-\xi)\delta(t-s)$. This is a broader modelling framework in which a correlation between the noise experienced by all particles—as in (2)—is *not* assumed. A principal computational advantage of this viewpoint is the ability to efficiently capture many stochastic realisations simultaneously when doing a forward simulation in time. For brevity, we will call (A2) an SDE driven by *uniform noise* and (3) driven by *nonuniform noise*, to refer to the fact that the noise realisation used in each simulation is uniform or nonuniform in the initial condition, respectively. In the remainder we use the term 'simulation' to express one implementation of (2) or (3) over a time interval, for a given collection of initial conditions.

The systems (2) and (3) can alternatively be thought of in the weak sense via the same [67] corresponding Fokker–Planck equation

$$\frac{\partial\rho}{\partial t} + \nabla\cdot(\rho v) = \frac{\varepsilon^2}{2}\nabla\cdot\nabla\cdot\left(\rho\,\sigma\sigma^\top\right), \qquad (4)$$

which encodes how densities $\rho(y,t)$ evolve under the flow.

Since solutions y to (2) or (3) are random processes, any entities analogous to stable/unstable manifolds of the deterministic system (1) are themselves random. There are well-established methods to account for stable/unstable manifold displacements due to *deterministic* perturbations using for example the Melnikov function [4]. Here, we extend this notion to stochastic perturbations.

We first consider stochastically perturbed unstable manifolds. For the deterministic flow, Γ^u is defined in terms of the set of points which approaches a as $t\to-\infty$. Thus, setting $\sigma(y,t)=0$ for $t<t_1$ is a technical trick which enables the identification of the random unstable manifold at time t_1 to be precisely Γ^u. Its continuation in time is then obtained by flowing *forward* in time from t_1 onwards. To formalise the definition, we first note that the deterministic unstable manifold Γ^u can be parametrised as a solution $x^u(t)$ of (1), where $x^u(t)\to a$ as $t\to-\infty$. (This highlights the necessity of requiring infinite times in order to define the unstable manifold Γ^u in the standard way for deterministic systems.) Thus, $\Gamma^u := \bigcup_{p\in\mathbb{R}} x^u(p)$. The *random unstable set* $G^u(t)$ is now defined by

$$G^u(t) := \bigcup_{p\in\mathbb{R}}\Big\{y^u(p,t) : y^u(p,t) \text{ solves } (2)/(3) \text{ with } y^u(p,t_1) = x^u(t_1-t+p)\Big\}. \qquad (5)$$

The initial condition $y^u(p,t_1)=x^u(t_1-t+p)$ is chosen to ensure that the time-evolved state $y^u(p,t)$ will be close to $x^u(p)$ at time t (for the deterministic case with $\sigma=0$ we would have $y^u(p,t)=x^u(p)$). Upon varying the initial condition $x^u(t_1-t+p)$ over p, the full deterministic unstable manifold Γ^u is used as the initial condition at time t_1. Since points on Γ^u at $t=t_1$ asymptote to a as $t\to-\infty$ (because there is no stochasticity imposed when $t<t_1$), so will points on $G^u(t)$ for any t. Thus, our definition complies with the notion of pullback attractors (see for example [29]). We note moreover that definition (5) is generalisable to the situation where the ODEs (1) is in $\mathbb{R}^n$, and the perturbed unstable set is associated with an (any-dimensional) unstable manifold of any invariant submanifold a, as long as the stochasticity is assumed to be zero for $t<t_1$.

Depending on whether the stochastic system employs uniform noise as in (2) or nonuniform noise as in (3) the unstable set $G^u(t)$ will have different characteristics. If the same noise realisation is used for every initial point on the manifold for each forward-time simulation as in (2), $G^u(t)$ will be a smooth curve for fixed time-slice t. Indeed, in this situation, it is possible to define $G^u(t)$ as

the random unstable *manifold* for (2), and there are many results which establish its smoothness in more generality [29, 30, 33–38]. We show in Fig. 2a a schematic for $G^u(t)$ (green curve) at a time instance t, in this situation.

On the other hand, if we use (3) to define the random unstable set $G^u(t)$, then it will not be smooth because each initial point $x^u(t_1 - t + p)$ experiences a different noise realisation in a forward-time simulation. We display in Fig. 2b a schematic of the set $G^u(t)$ in this case, bearing in mind that this is a finite representation of the uncountable number of points comprising $G^u(t)$. We note that while the random unstable set associated with uniform noise using (2) could be defined for infinite-time stochasticity using alternative methods [29–31, 33–38], it cannot be extended to infinite times in an obvious way for nonuniform noise using (3). Moreover, the actual computational construction of stochastic slow manifolds in the sense of [29] for the uniform noise case (2) is based on noise convolutions which involve unknown anticipating future noise terms. The most lucid construction is provided by a normal form transformation [32, 68] but requires knowledge of future unknown noise which may be heuristically replaced by additive noise terms. The restriction to a finite value of t circumvents this problem, suggesting a straightforward computational construction which works equally well for describing the statistics associated with random unstable sets for uniform and for nonuniform noise.

Next, we provide an analogous definition for the finite-time random stable set $G^s(t)$ for $t < t_1$. The stable manifold Γ^s is defined at time $t = t_1$ for the deterministic flow (1) by $\Gamma^s := \bigcup_{p\in\mathbb{R}} x^s(p)$, in which $x^s(t)$ is a solution to (1) obeying $x^s(t) \to a$ as $t \to \infty$. For the stochastic flow (2), we take Γ^s as an 'initial' condition at time t_1, and run (2) backwards in time to time t. This requires viewing the SDEs (2) and (3) as backward stochastic differential equations which, like their forward counterparts, have well-defined solutions over a finite time under certain smoothness assumptions [69]. Using this backwards time approach gives meaning that the random stable set $G^s(t)$ is the set of points which asymptotically approaches a as $t \to \infty$. We therefore define the *random stable set* $G^s(t)$ by

$$G^s(t) := \bigcup_{p\in\mathbb{R}} \Big\{ y^s(p,t) : y^s(p,t) \text{ solves (2)/(3)} \\ \text{with } y^s(p,t_1) = x^s(t_1 - t + p) \Big\}. \quad (6)$$

The set $G^s(t)$ will be either a smooth random stable manifold, or an uncountable collection of points depending on whether the noise is uniform as in (2) or nonuniform as in (3).

B. Uncertainty of stable/unstable sets

The random stable and unstable sets differ for each realisation of noise. To enable a statistical description of this variation, we characterise their mean and variance with respect to realisations of the driving Brownian noise. We first examine the uncertainty associated with the unstable set $G^u(t)$. While the geometric nature of the sets $G^u(t)$ is inherently different for uniform and nonuniform noise (cf. Figure. 2), our theory works in *either* case. To define the displacement from the deterministic manifold Γ^u, we fix $p \in \mathbb{R}$, and let

$$\hat{n}^u(p) := \frac{v^\perp\left(x^u(p)\right)}{\left|v\left(x^u(p)\right)\right|} \quad (7)$$

be the unit normal vector to Γ^u at the location $x^u(p)$. Here, the $\perp$ operation on vectors in $\mathbb{R}^2$ denotes rotation by $+\pi/2$, that is,

$$h^\perp := \begin{pmatrix} 0 & -1 \\ 1 & 0 \end{pmatrix} h\,. \quad (8)$$

Let $t > t_1$ be finite. For $y^u(p,t) \in G^u(t)$, we define the random normal displacement by

$$N^u(p,t) := [y^u(p,t) - x^u(p)] \cdot \hat{n}^u(p) \quad (9)$$

which represents the normal displacement of $G^u(t)$ with respect to Γ^u, at locations parametrised by p, and at times $t > t_1$. The reader is referred to Fig. 2 for a geometric depiction of the displacement.

We now look at the statistics of the displacement in terms of averaging over different realisations of the driving noise. To elucidate N^u's leading-order behaviour, we consider the random variable

$$\tilde{N}^u(p,t) := \lim_{\varepsilon\to 0} \frac{N^u(p,t)}{\varepsilon}\,. \quad (10)$$

By adapting the stochastic curve theory of [40], we show in Appendix A that the leading-order expectation of the normal displacement is zero, i.e.,

$$E\left[\tilde{N}^u(p,t)\right] = 0 \quad \text{for all } p, \quad (11)$$

where the expectation value is taken with respect to all Brownian driving paths. This relies on Itô's lemma [70, 71] being applied to (2) to determine the evolution equation for the random variable $y^u(p,t)$ to first-order. The mean over realisations of the unstable set $G^u(t)$ is therefore the deterministic unstable manifold Γ^u, independent of t.

Next, we define the standard deviation—a measure for the uncertainty—of the leading-order normal displacement by

$$w^u(p,t) := \sqrt{\mathrm{Var}\left[\tilde{N}^u(p,t)\right]}\,. \quad (12)$$

Appendix A shows that the methods of [40] (which rely on the Itô isometry [70, 71]) can be adapted to obtain

$$w^u(p,t) = \frac{\left[\int_{t_1}^{t} e^{2\int_\tau^t [\nabla\cdot v](x^u(\xi-t+p))\mathrm{d}\xi} \left|\sigma^\top(x^u(\tau-t+p),\tau)\, v^\perp\left(x^u(\tau-t+p)\right)\right|^2 \mathrm{d}\tau\right]^{1/2}}{\left|v\left(x^u(p)\right)\right|}\,, \tag{13}$$

in which $\sigma^\top$ is the transpose of the matrix σ. Thus, $\varepsilon w^u(p,t)$ gives an expression for the leading-order uncertainty of the normal displacement between $G^u(t)$ and Γ^u at a location p, and at a time-instance t. In contrast with the random variable $N^u(p,t)$, $w^u(p,t)$ is smooth in p even for nonuniform noise as in (3). We note that the expressions (11) and (13) work for *either of the interpretations (2) or (3)*, because in deriving the expressions, p is considered fixed (see Appendix A).

The uncertainty (13) associated with the unstable set monotonically increases with time t, representing the accumulation of stochastic effects as time progresses. However, under generic conditions (σ is bounded), we show in Appendix B that as t increases, $w^u(p,t)$ approaches a constant value at any particular point $x^u(p)$ on Γ^u, and does so exponentially fast. The saturation of the uncertainty of the flow barrier is related to approaching the invariant density of the corresponding Fokker–Planck system (4). If the time required to reach statistical equilibrium is less that the characteristic time scale τ_c of the large-scale flow, we may set in our formulæ $t \to \infty$. We numerically verify that this saturation occurs rapidly in the Taylor–Green example we analyse in Section IV.

The limit $p \to -\infty$ in (13) provides the uncertainty at the saddle point a. This limit is computed exactly as described in Section 3.5 of [72], where a similar limit is computed for a comparable expression (this argument is similar in spirit to that presented in Appendix B for the limit $t \to \infty$ as well). We find that

$$w^u(-\infty,t) = e^{\lambda_s t}\left(\int_{t_1}^{t} e^{-2\lambda_s \tau}\left|\sigma^\top(a,\tau)\,\hat{e}_u^\perp\right|^2 \mathrm{d}\tau\right)^{1/2}, \tag{14}$$

and this uncertainty is measured in the direction $\hat{e}_u^\perp$ from a (i.e., $\hat{n}^u(p) \to \hat{e}_u^\perp$ as $p \to -\infty$). The vectors $\hat{e}_s$ and $\hat{e}_u$ are the normalised eigenvectors of the Jacobian matrix $\nabla v(a)$ with corresponding eigenvalues $\lambda_s < 0$ and $\lambda_u > 0$, tangential to the stable and unstable manifolds at a, respectively. The appearance of the *complementary* eigenvalue λ_s when considering an uncertainty of the unstable manifold in the $v_u^\perp$ direction is to be noted.

Let us return to the general expression (13) for the uncertainty $w^u(p,t)$. There are two simplifications which occur under regularly considered cases:

(i) If the fluid is incompressible with $\nabla \cdot v = 0$, the entire exponential factor in (13) simplifies to 1.

(ii) If the diffusion is isotropic and independent of space and time, then $\sigma = \mathrm{Id}$ (but let us suppose it retains the appropriate dimensions). This allows the σ term to be discarded from (13). Moreover, since $\left|v^\perp\right| = |v|$, the $\perp$ symbol on the v in the integrand can be removed.

If *both* the above simplifications are in operation, then the uncertainty formula (13) reduces to the particularly simple form

$$w^u(p,t) = \frac{\left[\int_{t_1}^{t} \left|v\left(x^u(\tau-t+p)\right)\right|^2 \mathrm{d}\tau\right]^{1/2}}{\left|v\left(x^u(p)\right)\right|}\,. \tag{15}$$

This is the temporal L^2-norm of the quantity $\left|v\left(x^u(\tau-t+p)\right)\right| / \left|v\left(x^u(p)\right)\right|$, which represents the fractional speed at a time-varying point in relation to that at the final point $x^u(p)$ (occurring at $\tau = t$). The along-manifold velocity variations therefore impact the across-manifold uncertainties; an intuitive explanation is that the along-manifold velocity variation is directly linked to that across the manifold because of incompressibility.

If only simplification (ii) applies, the uncertainty at a, (14), is explicitly integrated to give

$$w^u(-\infty,t) = e^{\lambda_s t}\left(\frac{e^{-2\lambda_s t} - e^{-2\lambda_s t_1}}{-2\lambda_s}\right)^{1/2}, \tag{16}$$

and if additionally $\nabla\cdot v = 0$, the condition $\lambda_s = -\lambda_u$ can be applied.

The general expression for the standard deviation (13) allows for the definition of uncertainty regions around Γ^u. At any time-instance t, we define

$$R^u_\alpha(t) := \bigcup_p \left\{x^u(p) + \alpha r \varepsilon\, w^u(p,t)\hat{n}^u(p) \;:\; r \in [-1,1]\right\}. \tag{17}$$

The parameter α represents how many standard deviations around Γ^u the region is, and therefore R^u_α defines a region of uncertainty of the stochastic unstable sets $G^u(t)$, to leading-order in ε. While there is no obvious reason to expect that the unstable sets are normally distributed around the unstable manifold Γ^u (indeed, our numerics indicate that they are not), a choice $\alpha = 2$ (which would represent a 95% confidence interval for an assumed normal distribution) appears reasonable for capturing the bulk of the uncertainty.

An analogous characterisation is possible for the displacement of the random stable set $G^s(t)$. We define

$$\hat{n}^s(p) := \frac{v^\perp\left(x^s(p)\right)}{\left|v\left(x^s(p)\right)\right|} \tag{18}$$

and for $t < t_1$ consider

$$N^s(p,t) := \left[y^s(p,t) - x^s(p)\right]\cdot \hat{n}^s(p)\,, \tag{19}$$

As before, we expect $E\left[N^s(p,t)\right] = \mathcal{O}(\varepsilon)$, inspiring the definition

$$\tilde{N}^s(p,t) := \lim_{\varepsilon\to 0} \frac{N^s(p,t)}{\varepsilon}\,. \tag{20}$$

The proofs for the unstable manifold furnished in Appendix A go through for the stable manifold with no substantive change. In particular,

$$E\left[\tilde{N}^s(p,t)\right] = 0 \quad \text{for all } p, \tag{21}$$

implying that the mean of the stable sets over different realisations of the Brownian driving noise is given by the stable manifold Γ^s. The standard deviation defined by

$$w^s(p,t) := \sqrt{\mathrm{Var}\left[\tilde{N}^s(p,t)\right]}, \tag{22}$$

yields the uncertainty measure

$$w^s(p,t) = \frac{\left[\int_t^{t_1} e^{2\int_\tau^t [\nabla\cdot v](x^s(\xi-t+p))\mathrm{d}\xi} \left|\sigma^\top(x^s(\tau-t+p),\tau)\, v^\perp(x^s(\tau-t+p))\right|^2 \mathrm{d}\tau\right]^{1/2}}{|v(x^s(p))|}. \tag{23}$$

Our previous discussions on simplifications under incompressibility and isotropic diffusion for w^u apply equally for (23). Moreover, saturation of $w^s(p,t)$ is to be expected as $t \to -\infty$ for bounded σ. The uncertainty at a in the direction $\hat{e}_s^\perp$ is obtained by taking the limit $p \to \infty$ in (23), which leads to

$$w^s(\infty,t) = e^{\lambda_u t}\left(\int_t^{t_1} e^{-2\lambda_u \tau}\left|\sigma^\top(a,\tau)\,\hat{e}_s^\perp\right|^2 \mathrm{d}\tau\right)^{1/2}. \tag{24}$$

The corresponding expression under $\sigma = \mathrm{Id}$ is

$$w^s(\infty,t) = e^{\lambda_u t}\left(\frac{e^{-2\lambda_u t} - e^{-2\lambda_u t_1}}{2\lambda_u}\right)^{1/2}. \tag{25}$$

In general, the region of uncertainty is

$$R^s_\alpha(t) := \bigcup_p \{x^s(p) + \alpha r\varepsilon\, w^s(p,t)\hat{n}^s(p) \;:\; r \in [-1,1]\}, \tag{26}$$

which quantifies the fuzziness of the stable manifold when subjected to a (small) stochastic perturbation.

In the next two sections, we consider two specific examples. In the first example in Section III, we examine the perturbations to the stable manifold for uniform and nonuniform noise as in (2) and (3) for a velocity which is not area-preserving. Our focus here is directly on the manifolds and their uncertainty, but we will also compare our uncertainty measures to the spatial structure of a noise-averaged exponential stretching measure. In the second example, we study a stochastically perturbed area-preserving flow and show how our analytical expressions can be used to quantify fluid transport across stochastic Lagrangian structures. Specifically, this example relates our measures to spatial mixing regions near the stable manifold.

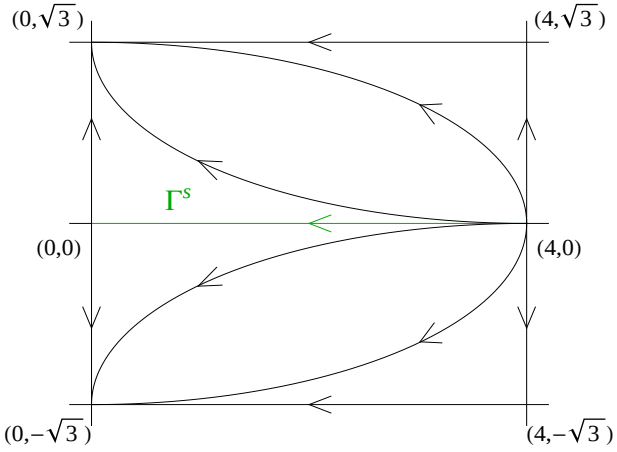

FIG. 3. The phase plane of (27), with the stable manifold of interest, Γ^s, shown in green.

III. STOCHASTIC SETS RESPECT EXPONENTIAL STRETCHING: A COMPRESSIBLE EXAMPLE

The base flow we consider for this example is given by

$$\left.\begin{aligned}\dot{x}_1 &= -4x_1 + x_1^2\\ \dot{x}_2 &= 3x_2 - x_2^3\end{aligned}\right\}, \tag{27}$$

which is *not* area-preserving. The part of the phase plane of interest to us is shown in Fig. 3. The focus shall be on the stochastic perturbation to the stable manifold Γ^s of $(0,0)$ as shown in magenta. The relevant parametric representation for this, as a solution to (27), is

$$x^s(p) = \begin{pmatrix} 4/\left(1+e^{4p}\right)\\ 0\end{pmatrix}; \quad p \in \mathbb{R}.$$

The analytical formula (23) for the uncertainty measure w^s along the stable curve requires the calculation of the

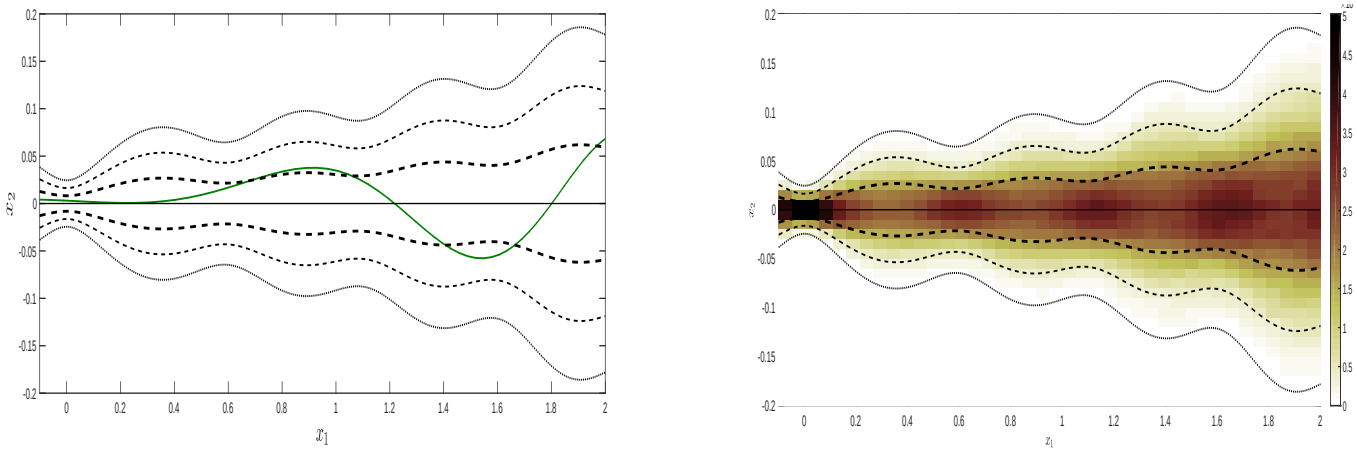

(a) (b)

FIG. 4. Smooth stable set $G^s(t=0)$ of the stochastic flow associated with (27) driven by uniform noise with $\varepsilon = 0.02$ from time $t_1 = 2$. (a): Single simulation (green). (b): Histogram from 100,000 simulations. The black curves depict the $\alpha = 1$ (thick dashed), $\alpha = 2$ (thin dashed) and $\alpha = 3$ (dotted) standard deviation envelopes $R^s_\alpha(t=0)$ (cf. (26) using the analytical expression (28) for $w^s(p,t)$).

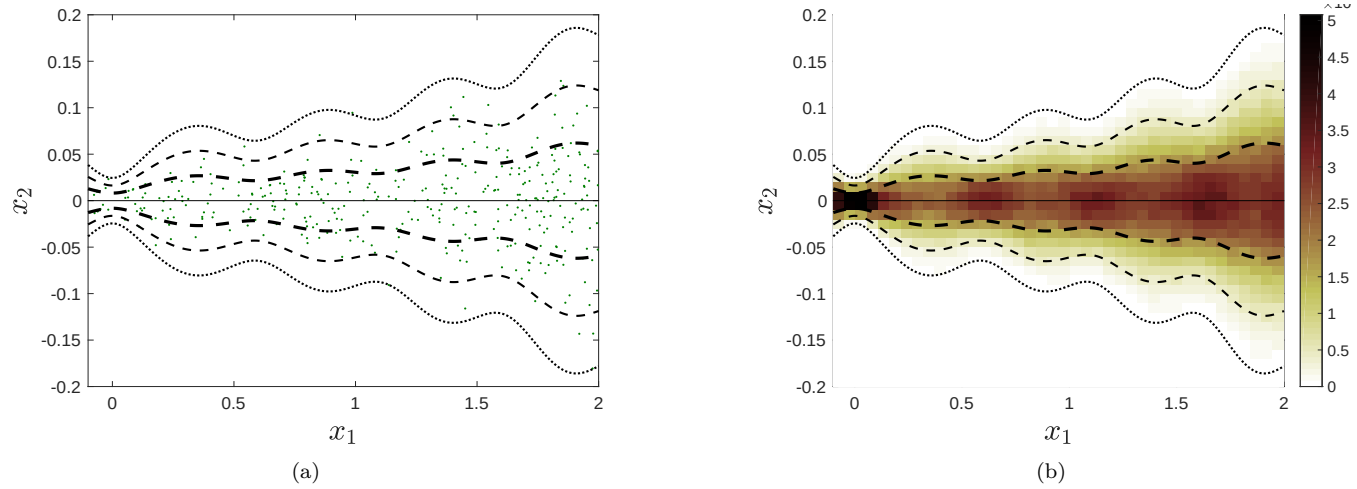

(a) (b)

FIG. 5. Stable set $G^s(t=0)$ of the stochastic flow associated with (3) driven by nonuniform noise with $\varepsilon = 0.02$ from time $t_1 = 2$. (a): Single simulation (green dots). (b): Histogram from 1000 simulations. The black curves depict the $\alpha = 1$ (thick dashed), $\alpha = 2$ (thin dashed) and $\alpha = 3$ (dotted) standard deviation regions $R^s_\alpha(t=0)$ (cf. (26) using the analytical expression (28) for $w^s(p,t)$).

quantities

$$v\left(x^s\left(\tau - t + p\right)\right) = \begin{pmatrix} -16e^{4(\tau-t+p)} / \left(1 + e^{4(\tau-t+p)}\right)^2 \\ 0 \end{pmatrix}$$

and

$$\left[\nabla \cdot v\right]\left(x^s(\tau - t + p)\right) = -1 + \frac{8}{1 + e^{4(\tau-t+p)}}\,.$$

After some algebra (not shown), the leading-order uncertainty of the stable manifold (23) reduces to

$$w^s(p,t) = e^{3t}\left(\int_t^{t_1} e^{-6\tau}\left[\sigma_{21}^2\left(\frac{4}{1+e^{4(\tau-t+p)}}, 0, \tau\right) + \sigma_{22}^2\left(\frac{4}{1+e^{4(\tau-t+p)}}, 0, \tau\right)\right]\mathrm{d}\tau\right)^{1/2}, \tag{28}$$

where σ_{ij} represent the components of the diffusion matrix. For the computations in this section, we choose

$$\sigma_{11} = 1\,,\ \sigma_{12} = 0\,,\ \sigma_{21} = x_2 - 1 \text{ and } \sigma_{22} = 3\sin\left(2\pi x_1\right) e^{0.8x_1}$$

which support a nontrivial dependency along the deter-

ministic stable manifold $x_2 = 0$.

We will now study the stable set $G^s(t)$ with $t_1 = 2$. To numerically solve the SDEs (2) and (3) we employ the Euler–Maruyama scheme [73, 74]. There are two competing issues in choosing ε and the time-step Δt for the numerical simulations: $\varepsilon\sqrt{\Delta t}$ must be much smaller than Δt (i.e., $|\varepsilon| \ll \sqrt{\Delta t}$) to ensure that the stochasticity appears as a perturbation, while Δt must itself be small for better accuracy of the method. In the following we use $\varepsilon = 0.02$ and $\Delta t = 0.01$ unless otherwise specified.

Let us first compute the stable curve $G^s(t = 0)$ for the system (27) driven by uniform noise, in which each initial condition is propagated with the same realisation of the noise as in (2). To do so, we seed 4000 particles along $y_2 = 0$, equally spaced between $x_1 = 0$ and 0.004 at time $t_1 = 2$, and advect (2) backward in time to $t = 0$. The stable curve $G^s(0)$ (green) associated with one single simulation is shown in Fig. 4 (a). We now show that the average behaviour of the stable curves $G^s(t)$ with respect to different realisations of the noise is well described by our theory, where the mean is given by Γ^s (up to $\mathcal{O}(\varepsilon^2)$) and the standard deviation by $w^s(p, t)$. In Fig. 4 (b), we present a histogram using 100,000 independent simulations (each seeded with 4000 initial particles), formed by counting the proportion of the 4×10^8 points within each bin of size (0.0525×0.01) in the displayed domain at time $t = 0$. It is clearly seen that the contour lines of the histogram align well with the regions $R^s_\alpha(0)$ of the uncertainty.

We next numerically generate the random stable set $G^s(t = 0)$ for the system (27) driven by nonuniform noise, as in the class of SDEs (3). Fig. 5 (a) shows $G^s(t = 0)$ obtained for a single simulation; it is now a collection of points as opposed to the smooth curve depicted in Fig. 4 (a). The histogram over realisations of the noise is shown in Fig. 5 (b) and resembles the histogram obtained for the SDE (2) driven by uniform noise shown in Fig. 4 (b). Note that the average is taken here only with 1000 realisations whereas in the uniform nosie case we used 100,000 realisations. As the Fokker–Planck equation (4) is identical for the two SDEs (2) and (3), we can interpret the simulation of the nonuniform noise case (3) as an effective computational tool to determine the statistical behaviour of an ensemble of realisations of the noise for the uniform noise case (2).

Our theory gives the mean and standard deviation of the instantaneous normal distance N^s of the stable curve $G^s(t)$ to the stable manifold Γ^s (cf. (19)). We now numerically verify these expressions, validating also that these expressions are correct to order ε. To determine the statistics of scatter around the point $(1.5, 0)$ on the stable manifold at time $t = 0$, we backwards advect from time $t_1 = 2$ from the point $(0.0006968, 0)$. This is the point from which $(1.5, 0)$ maps under deterministic advection from $t = 0$ to $t_1 = 2$, and is associated with $p = 0.12771$. Since we are considering only one initial condition, the systems (2) and (3) are equivalent for this experiment. The quantity N^s (in this case $N^s = x_2$ because $\hat{n}^s$ is the unit vector in the x_2-direction) is computed for each of $M = 10^4$ simulations. The empirical probability density function $f(N^s)$ is shown in Fig. 6 for several values of ε together with a normal probability density function with the mean and variance given by our theoretical predictions; the mean is zero according to (21) and the standard deviation $\varepsilon w^s(0.12771, 0)$ is computed from (23). The simulations also illustrate the interesting fact that the actual density function clearly does not converge to a Gaussian; in all our simulations we observed a sharper peak at zero. The spread of the density, however, clearly exhibits convergence as $\varepsilon \to 0$. Our theory provides an $\mathcal{O}(\varepsilon)$ expression for the standard deviation, and thus this value should be accurate up to $\mathcal{O}(\varepsilon^2)$. We explore this in Fig. 6 (d), where we use M simulations for each ε to plot the logarithm of the error

$$E = \left| \sqrt{\frac{1}{M} \sum_{j=1}^{M} \left(x_2^{(j)}(0) \right)^2} \; - \; \varepsilon w^s(0.12771, 0) \right| \qquad (29)$$

between the theoretical and numerical standard deviations against ε, where $x_2^{(j)}(0)$ is the x_2 coordinate at time $t = 0$ of the j^{th} ensemble member with initial condition $x_1(t_1) = 0.12771$ and $x_2 = 0$. In this region, the error appears to go as $\varepsilon^{2.5}$, confirming the scaling $\mathcal{O}(\varepsilon^2)$ as discussed above.

We next compute the finite-time Lyapunov exponent (FTLE) field, whose strong ridges help identify stable manifolds in the deterministic setting. Forward-time FTLE fields are the relevant diagnostics for stable manifolds, since particles on the stable manifold will be exponentially stretched apart by the complementary unstable manifold attached to $(0, 0)$ as visible in Fig. 3. The FTLEs at a time t are the finite time averages of the maximum expansion rate for a pair of particles propagated by (2) over the time interval $[t, t_1]$ (see, for example, [3] on the computation of FTLEs). Monte Carlo methods for FTLE fields are now emerging as a tool in stochastic situations [18, 19, 75–79]. Following these ideas, we seed 200×400 particles in the same domain displayed in Fig. 4 at time $t = 0$. The particles are then advected forward in time with the dynamics (2) to time $t_1 = 2$, and the resulting FTLE field is computed. Fig. 7(a) shows a clear ridge of the FTLE field, indicative of the stable manifold curve $G^s(t = 0)$. Exactly as for deterministic flows, this sharp ridge is an indication that for that particular realisation of noise, the stable curve is smooth. Since recent work legitimises taking the expectation over many simulations [79], in Fig. 7(b) we show the averaged FTLE field across 100,000 simulations, of which (a) is one. The statistical spread of the stretching fields displays a 'fattening' associated with the uncertainty of the stable set. We have used a nonlinear scaling on the colorbar to elucidate the variation in the (rarely visited) outer flanges, for an effective comparison with the theory even up to the three standard-deviation level. Our theoretical regions $R^s_\alpha(0)$ capture the undulating nature of the averaged FTLE field excellently, implying that the spa-

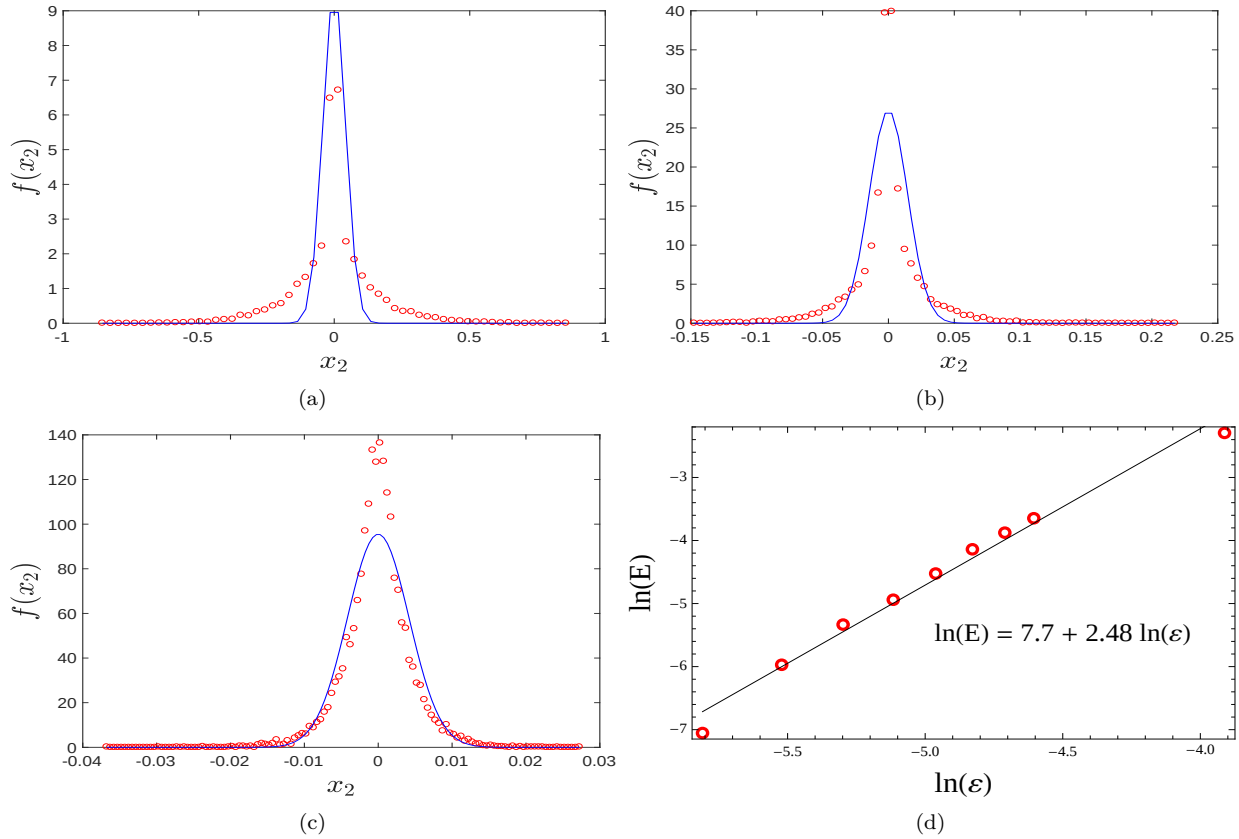

FIG. 6. (a-c) Analysis of the normal statistics of $N^s = x_2$ at the $(1.5, 0)$ for the stochastic flow associated with (27) driven by uniform noise from time $t_1 = 2$ to $t = 0$, for the values (a) $\varepsilon = 0.02$, (b) $\varepsilon = 0.007$ and (c) $\varepsilon = 0.002$. Shown is the empirical probability density function $f(N^s)$ of the simulation (red circles) using $M = 10^4$ simulations, and a reference normal probability density function with variance given by the theoretical values $\varepsilon w^s(0.12771, 0)$ as computed from (23) and mean zero as computed from (21) (blue curves). (d) The error E in the standard deviation versus ε in these simulations (red circles), in a log-log plot. The slope obtained by linear regression is 2.48.

tial structure of the exponential stretching statistics is well-explained by our theory.

We remark that performing the FTLE calculation using the nonuniform model (3) does not make sense, because the presence of *different* noise realisations in adjacent trajectories generate a flow map which is not smooth. The spatial gradients of the flow map then acquire large values which are additional to those arising from exponential separation.

IV. STOCHASTIC SETS GOVERN TRANSPORT: TAYLOR–GREEN FLOW

The previous example illustrated that the theory for the uncertainty of stochastic stable sets was consistent with both the actual stochastic evolution of a curve positioned on the stable manifold Γ^s at some final time, as well as the distribution of exponential stretching as quantified by FTLEs. We now explore the implications associated with the uncertainties to quantitatively understand *transport* across the deterministic flow barriers.

The deterministic base flow we examine here is the area-preserving Taylor–Green flow [4], also known as planar cellular flow,

$$\left.\begin{aligned} \dot{x}_1 &= -\sin(\pi x_1)\cos(\pi x_2) \\ \dot{x}_2 &= \cos(\pi x_1)\sin(\pi x_2) \end{aligned}\right\}. \tag{30}$$

Its phase portrait, which consists of a periodic array of counter-rotating vortices, is depicted inFig. 8. We wish to relate the uncertainty of the heteroclinic manifold (shown in green in Fig. 8) with the transport occurring between the upper and lower cell under stochastic perturbations. Particles within the cells get fed into the transport region by coming in towards the point $(1, 0)$ and then getting pulled along by this heteroclinic manifold; hence for the study of how particles are advected in forward time and diffuse across these two cells, it is their location with respect to the *unstable manifold* Γ^u which is pertinent.

We note that here $\nabla \cdot v = 0$, and moreover

$$x^u(p) = \begin{pmatrix} \frac{2}{\pi}\tan^{-1}(e^{-\pi p}) \\ 0 \end{pmatrix}$$

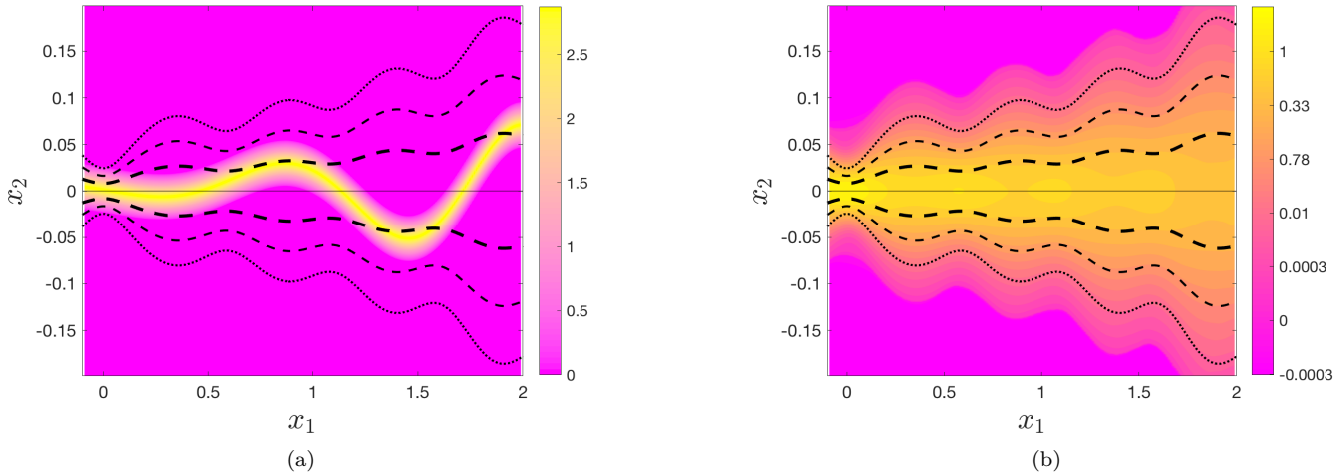

FIG. 7. The forward FTLE field computed at time $t = 0$ for the stochastic flow associated with (27) driven by uniform noise till time $t_1 = 2$, using identical conditions and notation as in Fig. 4. (a) One single simulation, and (b) The mean of 100,000 simulations using a nonlinearly-scaled colorbar. The black curves depict the $\alpha = 1$ (thick dashed), $\alpha = 2$ (thin dashed) and $\alpha = 3$ (dotted) standard deviation regions $R^s_\alpha(t = 0)$ (cf. (26) using the analytical expression (28) for $w^s(p, t)$).

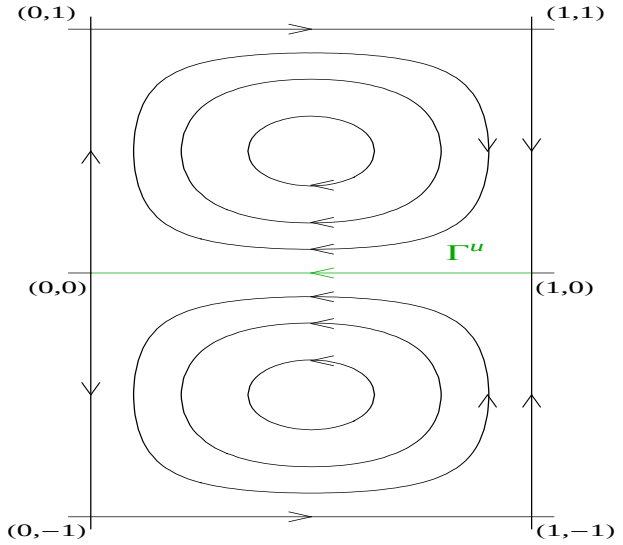

FIG. 8. The phase plane of the Taylor–Green flow (30), with the transport barrier between the upper and lower cell shown in green.

and

$$v\left(x^u\left(\tau-t+p\right)\right) = \begin{pmatrix} -2\,\mathrm{sech}\left[\pi\left(\tau-t+p\right)\right] \\ 0 \end{pmatrix}.$$

For general σ, performing the algebra on (13) leads to the fact that

$$w^u(p,t) = \frac{\left(\int_{t_1}^{t} \mathrm{sech}^2\left[\pi\left(\tau-t+p\right)\right]\left[\sigma_{21}^2\left(x_1(\tau-t+p),0,\tau\right)+\sigma_{22}^2\left(x_1(\tau-t+p),0,\tau\right)\right]\mathrm{d}\tau\right)^{1/2}}{\mathrm{sech}\left(\pi p\right)} \tag{31}$$

where

$$x_1(p) := \frac{2}{\pi}\tan^{-1}\left(e^{-\pi p}\right) \tag{32}$$

is the relationship between the x_1 coordinate along Γ^u and its p-parametrisation.

We examine the case $\sigma = \mathrm{Id}$, in which case (31) can be integrated explicitly to yield

$$w^u(p,t) = \cosh\left(\pi p\right)\left(\frac{\tanh\left[\pi p\right]-\tanh\left[\pi\left(t_1-t+p\right)\right]}{\pi}\right)^{1/2}.$$

After using the relationship (32) to represent w^u in terms of the location $x_1 \in (0,1]$ along Γ^u rather than p, the *explicit* uncertainty measure is evaluated as

$$\tilde{w}^u(x_1,t) := w^u(p,t) = \frac{1}{\sqrt{\pi\left(\coth\left[\pi\left(t-t_1\right)\right]-\cos\left(\pi x_1\right)\right)}}. \tag{33}$$

This is not zero as $x_1 \to 1$, and the limiting value coincides with the unstable manifold uncertainty expression $w^u(-\infty,t)$ 'at saddle-point' given in (14). However, $\tilde{w}^u$ becomes unbounded as $x_1 \to 0^+$, influenced by the stable manifold at $(0,0)$. This can be understood by realising that any small perturbation near $x_1 \gtrsim 0$ will be impacted by the strong exponential stretching in backward time due to the unstable manifold. Another interesting observation is that $\tilde{w}^u$ in (33) is monotonically increasing in t at each fixed location x_1 (representing an increase in uncertainty with time), but saturates rapidly to

$$\tilde{w}^u(x_1,\infty) = \frac{1}{\sqrt{2\pi}}\csc\left(\frac{\pi x_1}{2}\right), \tag{34}$$

defining a *long-term uncertainty* with respect to the location x_1 on Γ^u. This is a special case of the expected convergence to a limiting long-term uncertainty as shown in Appendix B. The existence of a constant limiting long-term uncertainty reflects the fact that the number of particles leaving a cell equals on average the number of particles entering a cell, allowing for a statistical equilibrium.

We now relate these expressions for the uncertainty to mixing. Specifically, we focus on the fact that, in the absence of stochasticity, the unstable manifold Γ^u forms a flow barrier between the upper and lower cells in Fig. 8. Fluid which swirls around in each cell and approaches $x_2 = 0$ from near $x_1 = 1$, remains separated by Γ^u as it travels near $x_2 = 0$. The inclusion of stochasticity destroys the 'flow barrier', thereby causing mixing between the fluids of the upper and lower cells. The spatial distribution of this mixing is directly controlled by the uncertainty regions R^u_α given by our theory, as we now verify. For our numerical verification, we seed the entirety of the upper cell with a uniform grid of 1000×2000 particles at time $t_1 = 0$, and advect it with the *stochastically perturbed* flow (with $\sigma = \mathrm{Id}$ and $\varepsilon = 0.1$), using the Euler–Maruyama scheme with $\Delta t = 0.01$. To obtain an efficient statistical description, we choose the SDE driven by nonuniform noise (3) rather than (2) driven by uniform noise, and perform only *one* simulation. In effect we perform a Monte–Carlo approximation of the Fokker–Planck equation (4) with the initial density being the Lebesgue measure on the two cells. (We cross-validated this computation by directly simulating the Fokker-Planck equation (4) using a spectral scheme with Crank-Nicolson time-stepping, using each as our initial density each of (i) uniform density in the top cell, (ii) uniform density in the bottom cell, and (iii) Dirac density supported on Γ^u (not shown).)

Since our focus is on particles which escape into the lower cell, we use periodic boundary conditions for $x_1 \in [0,1]$ to ensure that particles escaping from the left- and right-sides are fed back into the cell. We focus on a mixing zone near $x_2 = 0$, in particular choosing the region $(x_1,x_2) \in [0.1,0.9] \times [-0.1,0.1]$ (we exclude regions near $x_1 = 0$ and 1 to minimise periodic boundary condition effects). We bin this region into boxes of width 0.025 and height 0.005. We show in Fig. 9 (a) the histogram of the particles at time $t = 2$ which were initially at $t_1 = 0$ in the upper cell. The dashed blue curves are the $\alpha = 1$ (thick) and $\alpha = 2$ (thin) standard deviation envelopes of $R^u_\alpha(t)$ computed using (33); that is, the curves $x_2 = \pm\varepsilon\tilde{w}(x_1,t)$ (thick) and $x_2 = \pm 2\varepsilon\tilde{w}(x_1,t)$ (thin). These curves, which demarcate the uncertainty around the mean of the unstable set, align well with the density contour lines of the simulation. The larger density in the upper-right region is associated with regions well-divorced from the mixing region, that is outside the uncertainty region $R^u_\alpha(t)$. The 'leakage' of the upper fluid into the lower cell is seen to be spatially correlated with the fact that the uncertainty region $R^u_\alpha(t)$ extrudes into the lower cell. Moreover, the fact that the uncertainty region $R^u_\alpha(t)$ also ventures into the upper cell is displayed by the fact that there is a smaller density in the region defined by $R^u_\alpha(t)$ about $x_2 = 0$ in comparison to regions well above $x_2 = 0$. Fig. 9 (b) is a similar histogram, but now of the *lower* fluid, i.e., particles seeded uniformly in the lower cell at time $t_1 = 0$, and advected stochastically until $t = 2$. Once again, the ability of the uncertainty regions of the unstable set to describe the probability density function of the fluid particles is apparent.

To further quantify *mixing* between the cells, we define a covariance-like quantity as follows. Let u_i and l_i represent the number of 'upper' and 'lower' fluid particles which are in bin i at time t, and $\bar{u}$ and $\bar{l}$ be the average number of particles in each bin, with the average taken over all the bins in our mixing zone. Then we define the covariance function

$$c_i(t) := \left(u_i(t) - \bar{u}(t)\right)\left(l_i(t) - \bar{l}(t)\right) \tag{35}$$

for each cell i. One or the other of the two terms in (35) is close to zero in regions in which only one of the fluid types dominate, and therefore c_i is expected to be small in such regions. In contrast, c_i will be larger in regions in which *both* fluid types are present, i.e., regions of strong mixing between upper and lower fluids. The histogram of $c_i(2)$ is shown in Fig. 9 (c). As expected, the spatial distribution of the mixing measure c_i is indeed strongly impacted by the uncertainty envelopes of the unstable set. The dashed blue curves identifying $R^u_{\alpha=1}(t)$ do indeed appear to align with these contours of the covariance. That is, we have verified that the uncertainty measure $R^u_\alpha(t)$ quantifies the spatial mixing regions between cells.

Next, we analyse the temporal evolution of the mixing. Fig. 10 shows the covariance function $c_i(t)$ as a function of the final time t. The solid green curves drawn in each figure are the curves $x_2 = \pm\varepsilon\tilde{w}^u(x_1,\infty)$, with the saturated variance of the unstable set $\tilde{w}^u(x_1,\infty)$ as given in (34). At each time pictured in Fig. 10, the blue dashed

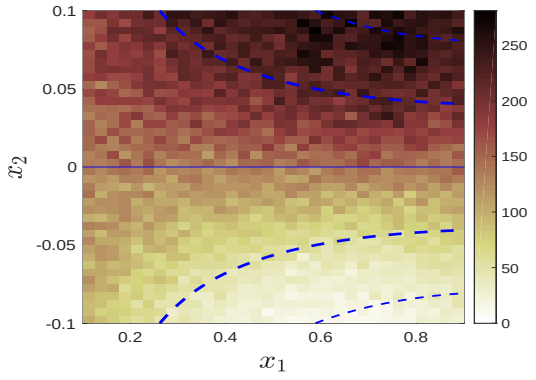

(a)

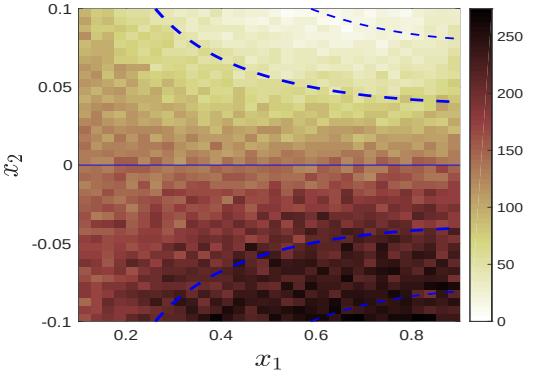

(b)

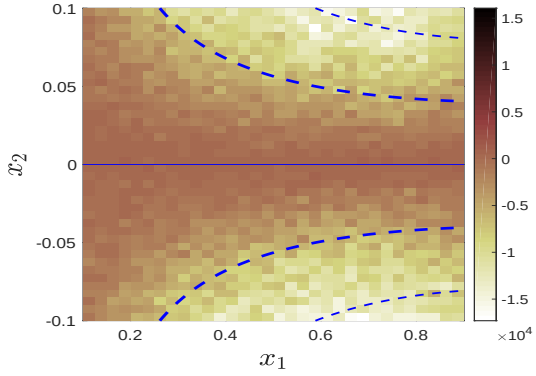

(c)

FIG. 9. Mixing characterization of Taylor–Green flow from time $t_1 = 0$ to $t = 2$, using uniformly seeded particles in the upper and lower cells. In all cases, the blue dashed lines depict the $\alpha = 1$ (thick) and $\alpha = 2$ (thin) standard deviation envelopes $R^u_\alpha(t)$ computed using (33). (a) Upper fluid histogram, (b) Lower fluid histogram, (c) Histogram of the covariance function $c_i(t = 2)$ as given in (35).

curves $R^u_\alpha(t)$ (for each t) describe the spatial variation of the covariance (35) remarkably well. As time increases, the increase in uncertainty is captured by the fact that the blue dashed curves are progressing outwards. However, this increase in uncertainty saturates rapidly with time. Specifically, $R^u_{\alpha=1}(t)$ appears to have converged by $t = 1$ to the green curves, which mark the saturation. Moreover, the dominant characteristics of the covariance contours at $t = 1$ are not very different from those at $t = 7$, and in both these situations the thick blue dashed curves associated with $R^u_{\alpha=1}(t)$ are virtually indistinguishable from the solid green curve representing the saturated variance around the unstable manifold Γ^u.

Finally, we illustrate that our theory also describes the spatial mixing for diffusion matrices which are temporally and spatially varying. We choose here

$$\left.\begin{aligned} &\sigma_{11} = 1\,,\ \sigma_{12} = 0\,,\ \sigma_{21} = 0 \quad \text{and} \\ &\sigma_{22} = \operatorname{sech}\left(x_1 - \tfrac{1}{2}\right)\cos\left(5\pi x_1\right)\tanh\left(t\right) \end{aligned}\right\}\,. \tag{36}$$

In this case, an explicit expression as in (34) for the saturated uncertainty cannot be given. However, it can be numerically computed using (31) for $t \gg 1$. Fig. 11 displays the covariance field $c_i(t)$. The highly-mixing region expands from being compressed near $x_2 = 0$ at $t = 0.1$, and saturates as expected (at a slower rate than for $\sigma = \mathrm{Id}$). The spatial variation of the uncertainty region $R_\alpha(t)$ at each time t, and its temporal evolution describes the numerically observed spatial mixing remarkably well.

V. DISCUSSION AND OUTLOOK

We have developed a framework to study the effect of small stochastic noise on the transport and mixing properties of two-dimensional fluid flow situations. We considered the idealised situations of a well-defined slowly varying large-scale flow subjected to small-scale noise, where have access to the associated stable and unstable manifolds at some fixed time. We extended the notion of stable and unstable invariant manifolds to noisy stable and unstable sets, by tracking the evolution respectively in backward and forward time. These sets are smooth curves for stochastic dynamical systems which employ the same noise realisation for each initial condition, but are an uncountable collection of points when each initial condition is evolved with its own Brownian noise driver. The mean and variance of the displacement of these curves from the associated deterministic stable and unstable manifolds at any finite time are characterised, in the presence of small noise. The mean displacement is, to leading-order in the noise parameter, zero, consistent with the heuristic expectation that the mean stable/unstable sets remain close to their deterministic counterparts. The variance is a measure of the fuzziness of these stable and unstable sets and quantifies how different realisations of the noise vary around the mean. As such, we provide an easily expressible theoretical quantification of statistical properties of the random stable/unstable manifolds. The theory can also be applied for an *unsteady* velocity field $v(x, t)$ as long as we are able to identify the stable/unstable manifold at a given time t_1. In other words, the theory works to quan-

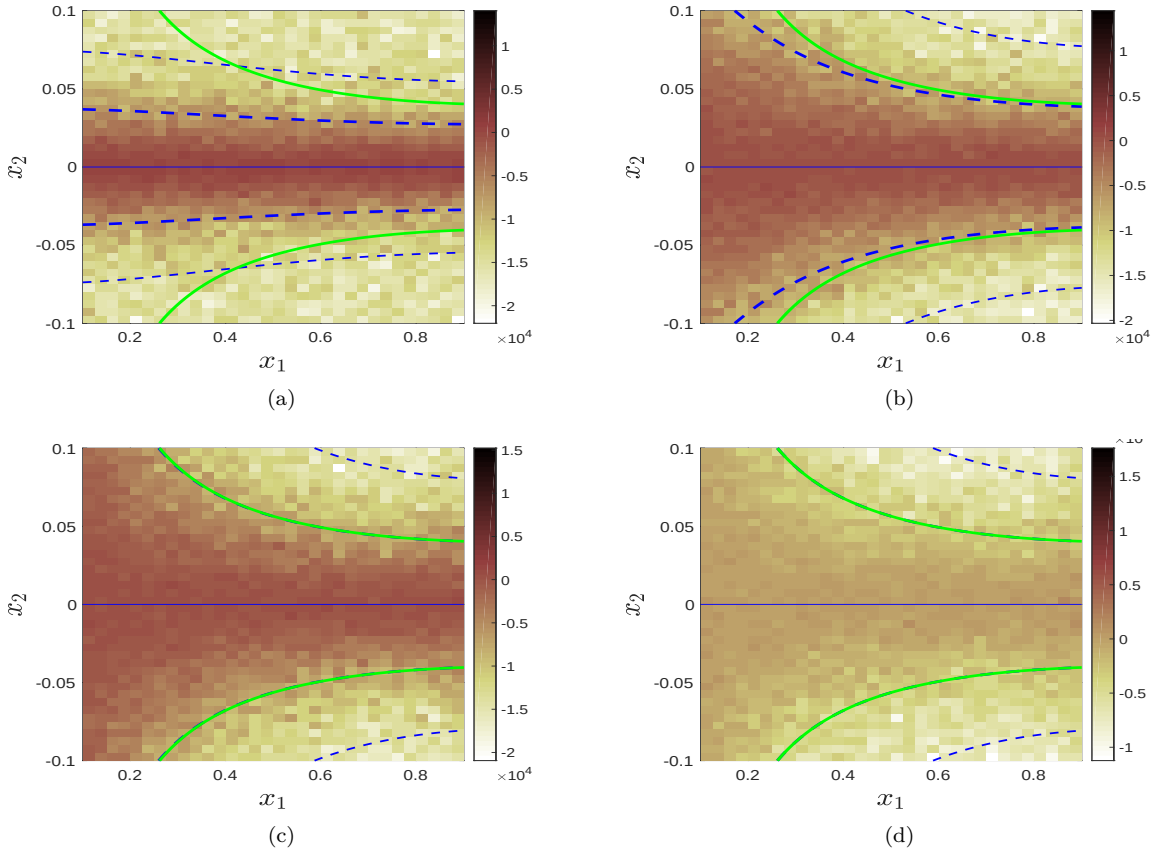

FIG. 10. Mixing characterisation of Taylor–Green flow from time $t_1 = 0$, using the contours of the covariance $c_i(t)$ (cf. (35)), with parameters and curve descriptions as in Figure 9. The final times for the figures are (a) $t = 0.1$, (b) $t = 0.4$, (c) $t = 1$ and (d) $t = 7$. The solid green curve represents the saturated uncertainty as defined by (34), to which $R^u_{\alpha=1}(t)$ is seen to converge as t increases.

tify the uncertainty due to *propagation*, assuming that at an initial time, the manifold is known.

We validate in numerical simulations that the coherent sets identified by the mean of the stable and unstable sets coincide with the ridges of the FTLEs. Whereas this is well established in the deterministic context, the application of FTLEs in the stochastic, or equivalently diffusive [18, 77, 78], context is less well explored. Moreover the variance theory that we developed was shown to capture the spatial structure of the averaged FTLE field, thereby providing an explicit method for ascribing an uncertainty in the location of ridges.

From a practical perspective, our formulæ quantify the expected transport of Lagrangian tracers across stochastically perturbed transport barriers. In particular, we use the variance of stable and unstable sets around their mean to determine the physical region in space which on average will be mixed at a given time. These well-defined mixing regions $R_\alpha(t)$ allow us to specify, via α, the probability of finding mixing and leakage across the mean of the stable and unstable sets. This can be used to determine, for example, the possible extent of environmental pollution such as oil spills, together with an uncertainty quantification based on any given model for the diffusivity matrix σ.

The analytical expressions we found require knowledge about the deterministic vector field as well as the diffusive behaviour (for example by means of eddy dispersion, drifter separation or alternative model for stochasticity [80–83]). Conversely, information about the extent of the mixing region and the fuzziness of the transport barriers may allow us to find estimates on the diffusion tensor given only measurements of the mean flow and the mixing region. This can be used to cross-validate the estimation of the diffusion tensor by oceanographers using eddy dispersion or drifter separation. Although this does not allow for the determination of each individual component of the diffusion tensor, the estimation of the variance allows for the estimation of the diffusivity across the mean stable and unstable curves. In the case presented in Section IV the formula (31) for the width of the transport barrier allows to determine, for example, $\sigma_{12}^2 + \sigma_{22}^2$.

Acknowledgments: We thank Tony Roberts for numerous stimulating discussions and his generous sharing of his expertise. The authors acknowledge partial support from the Australian Research Council: SB

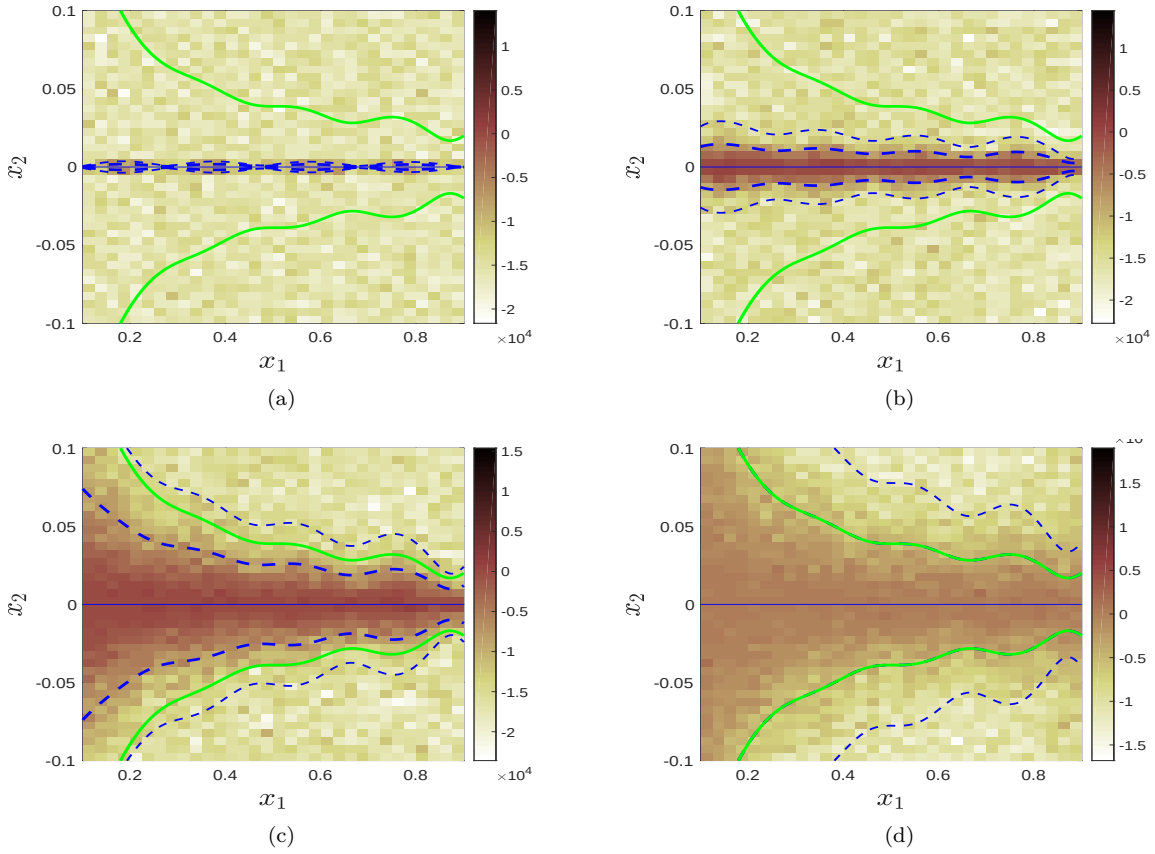

FIG. 11. Exactly as in Fig. 10, the covariance $c_i(t)$ is shown for the temporally and spatially varying diffusion σ as defined in (36) rather than $\sigma = \mathrm{Id}$. The final times are (a) $t = 0.1$, (b) $t = 0.4$, (c) $t = 1$ and (d) $t = 7$.

through grants FT130100484 and DP170100277, and GAG through grant DP180101385.

Appendix A: Proof of the the expectation and uncertainty expressions (11) and (13)

It will be necessary to first describe the results obtained in [40] in the notation of the present paper. The idea in [40] is to determine the difference between an advected curve of

$$\dot{x} = v(x,t) \tag{A1}$$

and

$$\mathrm{d}y = v(y,t)\mathrm{d}t + \varepsilon\sigma(y,t)\mathrm{d}W_t \tag{A2}$$

from the time t_1 to a general time t. The initial condition (at time t_1) for both equations is a curve $\mathcal{C}$ given parametrically by $x(q,t_1)$ where q is a parameter, and *any* parametric representation is permitted. Let $x(q,t)$ represent the final advected curve at time t according to the deterministic advection (A1), and $y(q,t)$ be the stochastically advected curve according to (A2), subject to the condition $y(q,t_1) = x(q,t_1)$. From this point onwards, we treat q as *fixed*. Define a moving normal on the deterministic curve at a general time $\tau \in [t_1, t]$ by

$$\hat{n}(q,\tau) := \frac{\partial x(q,\tau)}{\partial q} \Big/ \left|\frac{\partial x(q,\tau)}{\partial q}\right|$$

and the normal displacement at time t by

$$N(q,t) := [y(q,t) - x(q,t)] \cdot \hat{n}(q,t)\,.$$

Then, using an application of Itô's lemma, it was shown in [40] that

$$N(q,t) = \frac{\varepsilon \int_{t_1}^{t} e^{\int_\tau^t [\nabla\cdot v](x(q,\xi),\xi)\mathrm{d}\xi} \left(\left[\frac{\partial x(q,\tau)}{\partial q}\right]^\perp\right)^\top \sigma\left(x(q,\tau),\tau\right)\mathrm{d}W_\tau}{\left|\frac{\partial x(q,t)}{\partial q}\right|},$$

to leading-order in ε. It is immediately clear that $E\left[N(q,t)\right]/\varepsilon = 0$, since the integrand is of a deterministic function with respect to Brownian motion and yields zero [70, 71], and thus (11) will result. Moreover, it is shown in [40] with the help of the Itô isometry [70, 71] that

$$\sqrt{\mathrm{Var}\left[N(q,t)\right]} = \frac{\varepsilon\left(\int_{t_1}^{t} e^{2\int_\tau^t [\nabla\cdot v](x(q,\xi),\xi)\mathrm{d}\xi}\left|\sigma^\top\left(x(q,\tau),\tau\right)\left(\frac{\partial x(q,\tau)}{\partial q}\right)^\perp\right|^2 \mathrm{d}\tau\right)^{1/2}}{\left|\frac{\partial x(q,t)}{\partial q}\right|}\,, \tag{A3}$$

to leading-order in ε. The task is to now convert (A3) into (13), since slightly different conditions are in operation in this paper. The first is that v is steady; this is easily implemented by simply neglecting the second argument of v. The more subtle issue is to decide on the proper parametrisation for $\mathcal{C}$ (which is parametrised by q in the form $x(q,t_1)$), which in the present context must be the unstable manifold Γ^u. We know that the trajectory $x^u(p)$ parametrises Γ^u, and so we define for $\tau \in [t_1, t]$

$$x(q,\tau) := x^u(\tau - t + p)\,. \tag{A4}$$

Therefore, $x(q,t_1) = x^u(t_1 - t + p)$, and thus we set $q = p + t_1 - t$ as the (linear) relationship between the q and the p parametrisations. In fact, this is the reason why x^u in the definition for G^u in (5) is associated with the argument $t_1 - t + p$, i.e., q. Differentiating (A4), we get

$$\frac{\partial x(q,\tau)}{\partial q} = \frac{\partial x^u(\tau - t + p)}{\partial p} = v\left(x^u(\tau - t + p)\right)\,,$$

where we have used the fact that x^u is a solution to (1). Therefore, $\partial x/\partial q$ can simply be replaced by v (with appropriate arguments as obtained from the above expression) in (A3). Because of the definition (10), what is shown in (13) is the $\mathcal{O}(\varepsilon)$ term of (A3), and thereby (13) has been derived. We note in particular that this works at each fixed p.

The results of (21) and (23) associated with stochastic perturbations to the stable manifold Γ^s are similarly derived; here the main difference is that the curve $\mathcal{C}$ is Γ^s instead and we need to propagate backward in time. Hence we take $x(q,\tau) = x^s(\tau - t + p)$ for $\tau < t_1$, and we relate the parameters by $q = p + t_1 - t$ because $x(q,t_1) = x^s(t_1 - t + p)$.

Appendix B: Saturation of uncertainty expression (13)

Here, we provide a quick heuristic justification for our claim that if the diffusion matrix σ is bounded, the uncertainty (13) saturates as t increases. In examining (13) at large t, we observe that $x^u(\tau - t + p) \to a$. Indeed, for large t it is true that

$$x^u(\tau - t + p) \sim a + c\, e^{\lambda_u(\tau - t + p)}\hat{e}_u\,,$$

for some constant c (reflecting a choice of the parametrisation along Γ^u). Then, $v\left(x^u(\tau - t + p)\right)$ is simply the τ-derivative of this, and so

$$v\left(x^u(\tau - t + p)\right) \sim c\lambda_u e^{\lambda_u(\tau - t + p)}\hat{e}_u\,.$$

Next, we observe that as $t \to \infty$, $\nabla \cdot v \to \lambda_s + \lambda_u$, which is the value at the fixed point a. Inserting all these approximations into (13) yields

$$\begin{aligned} w^u(p,t) &\sim \frac{\sqrt{\int_{t_1}^t e^{2(\lambda_s+\lambda_u)(t-\tau)}\left|\sigma^\top(x^u,\tau)c\lambda_u e^{\lambda_u(\tau-t+p)}\hat{e}_u^\perp\right|^2\mathrm{d}\tau}}{\left|v\left(x^u(p)\right)\right|} \\ &\sim \frac{c\lambda_u e^{\lambda_u p}\sqrt{e^{2\lambda_s t}\int_{t_1}^t e^{-2\lambda_s\tau}|\sigma^\top(x^u(\tau-t+p),\tau)\,\hat{e}_u^\perp|^2\mathrm{d}\tau}}{c\lambda_u e^{\lambda_u p}} \\ &\le K\sqrt{e^{2\lambda_s t}\int_{t_1}^t e^{-2\lambda_s\tau}\,\mathrm{d}\tau} = K\sqrt{\frac{1 - e^{2\lambda_s(t-t_1)}}{-2\lambda_s}}\,. \end{aligned} \tag{B1}$$

In the above formal computations, we have assumed a bound K for σ, and demonstrated that $w^u(p,t)$ remains bounded as t increases (note the exponential decay because $\lambda_s < 0$). In general $w^u(p,t)$ will saturate towards a p-dependent value arising from the presence of $x^u(\tau - t + p)$ in the integrand.

[1] G. Haller, Lagrangian Coherent Structures, Annu. Rev. Fluid Mech. 47 (2015) 137–162.

[2] T. Peacock, J. Dabiri, Introduction to focus issue: Lagrangian coherent structures, Chaos 20 (2010) 017501.

[3] S. Shadden, Lagrangian coherent structures, in: R. Grigoriev (Ed.), Transport and mixing in laminar flows: from microfluidics to oceanic currents, Wiley, 2011.

[4] S. Balasuriya, Barriers and transport in unsteady flows: a Melnikov approach, Vol. 21 of Mathematical Modeling and Computation, Society for Industrial and Applied Mathematics (SIAM), Philadelphia, 2016.

[5] G. Froyland, Dynamic isoperimetry and the geometry of Lagrangian coherent structures, Nonlinearity 28 (2015) 3587–3622.

[6] S. Prants, M. Uleksky, M. Budyansky, Lagrangian oceanography: large-scale transport and mixing in the ocean, Springer, 2017.

[7] S. Balasuriya, Dynamical systems techniques for enhancing microfluidic mixing, J. Micromech. Microeng. 25 (2015) 094005.

[8] I. Mezić, S. Loire, V. Fonoberov, P. Hogan, A new mixing diagnostic and Gulf oil spill movement, Science 330 (2010) 486–489.

[9] G. Froyland, R. Stuart, E. van Sebille, How well connected is the surface of the global ocean?, Chaos 24 (2014) 033126.

[10] M. Allshouse, G. Ivey, R. Lowe, N. Jones, C. Beegle-Krause, J. Xu, T. Peacock, Impact of windage on ocean surface Lagrangian coherent structures, Environ. Fluid Mech. 17 (2016) 473–483.

[11] F. d'Ovidio, S. D. Monte, S. Alvain, Y. Dandonneau, M. Lévy, Fluid dynamical niches of phytoplankton types, Proc. Nation. Acad. Sci. 107 (2010) 18366–18370.

[12] F. Lekien, S. Ross, The computation of finite-time Lyapunov exponents on unstructured meshes for non-Euclidean manifolds, Chaos 20 (2010) 017505.

[13] D. Schmale, S. Ross, Highways in the sky: scales of atmospheric transport of plant pathogens, Annu. Rev. Phytopathology 53 (2015) 591–611.

[14] B. Knutson, W. Tang, P. Chan, Lagrangian coherent structure analysis of terminal winds: three-dimensionality, intramodel variations and flight analyses, Adv. Meteorol. 2015 (2015) 816727.

[15] R. Ni, N. Ouellette, G. Voth, Alignment of vorticity and rods with Lagrangian fluid stretching in turbulence, J. Fluid Mech. 743 (2014) R3.

[16] A. Thurnherr, A practical assessment of the errors associated with full-depth LADCP profiles obtained using tekedyne RDI workhorse aoustic Doppler current profilers, J. Atmos. Oceanic Tech. 27 (2010) 1215–1227.

[17] P. Berloff, J. McWilliams, Material transport in oceanic gyres. part II: hierarchy of stochastic models, J. Phys. Oceanography 32 (2002) 797–830.

[18] A. BozorgMagham, S. Ross, Atmospheric Lagrangian coherent structures considering unresolved turbulence and forecast uncertainty, Commun. Nonlin. Sci Numer. Simulat. 22 (2015) 964–979.

[19] D. Carlson, E. Fredj, H. Gildor, V. Rom-Kedar, Deducing an upper bound to the horizontal eddy diffusivity using a stochastic Lagrangian model, Environ. Fluid Mech. 10 (2010) 499–520.

[20] E. Mémin, Fluid flow dynamics under location uncertainty, Geophys. Astrophys. Fluid Dyn. 108 (2) (2014) 119–146. doi:10.1080/03091929.2013.836190.

[21] D. D. Holm, Variational principles for stochastic fluid dynamics, Proc. Roy. Soc. A. 471 (2176) (2015) 20140963, 19.

[22] E. Resseguier, E. Mémin, B. Chapron, Geophysical flows under location uncertainty, Part I: Random transport and general models, Geophys. Astrophys. Fluid Dyn. 111 (3) (2017) 149–176.

[23] E. Resseguier, E. Mémin, B. Chapron, Geophysical flows under location uncertainty, Part II: Quasigeostrophic models and efficient ensemble spreading, Geophys. Astrophys. Fluid Dyn. 111 (3) (2017) 177–208.

[24] E. Resseguier, E. Mémin, B. Chapron, Geophysical flows under location uncertainty, Part III: SQG and frontal dynamics under strong turbulence, Geophys. Astrophys. Fluid Dyn. 111 (3) (2017) 209–227.

[25] C. Cotter, G. A. Gottwald, D. Holm, Stochastic partial differential fluid equations as a diffusive limit of deterministic Lagrangian multi-time dynamics, arXiv:1706.00287.

[26] I. Melbourne, A. Stuart, A note on diffusion limits of chaotic skew-product flows, Nonlinearity 24 (2011) 1361–1367.

[27] G. A. Gottwald, I. Melbourne, Homogenization for deterministic maps and multiplicative noise, Proceedings of the Royal Society A: Mathematical, Physical and Engineering Science 469 (2013) 20130201.

[28] D. Kelly, I. Melbourne, Deterministic homogenization for fast–slow systems with chaotic noise, Journal of Functional Analysis 272 (10) (2017) 4063 – 4102.

[29] L. Arnold, Random dynamical systems, Springer Monographs in Mathematics, Springer-Verlag, Berlin, 1998.

[30] T. Wanner, Linearization of random dynamical systems, in: C. Jones, U. Kirchgraber, H. Walther (Eds.), Dynamics Reported, Vol. 4, Springer-Verlag, 1995, pp. 203–269.

[31] A. Roberts, Model emergent dynamics in complex systems, Mathematical Modeling and Computation, SIAM Press, 2015.

[32] A. Roberts, Normal form transforms separate slow and fast modes in stochastic dynamical systems, Phys. A 387 (1) (2008) 12–38.

[33] J. Duan, An introduction to stochastic dynamics, Cambridge Texts in Applied Mathematics, Cambridge University Press, New York, 2015.

[34] J. Duan, K. Lu, B. Schmalfuß, Smooth stable and unstable manifolds for stochastic evolutionary equations, J. Dyn. Differential Equations 16 (2004) 949–972.

[35] S.-E. Mohammed, M. Scheutzow, The stable manifold theorem for stochastic differential equations, Annals Prob. 27 (1999) 615–652.

[36] B. Schmalfuß, Attractors for non-autonomous dynamical systems, in: Proceeding EQUADIFF99, World Scientific, 2000, pp. 684–690.

[37] J. Li, K. Lu, P. Bates, Normally hyperbolic invariant manifolds for random dynamical systems: Part I - persistence, Trans. Amer. Math. Soc. 365 (2013) 5933–5966.

[38] N. Berglund, B. Gentz, Noise-induced phenomena in slow-fast dynamical systems: A sample-paths approach, Probability and its Applications (New York), Springer-Verlag London, Ltd., London, 2006.

[39] J. Pedlosky, Geophysical fluid dynamics, Springer, New York, 1987.

[40] S. Balasuriya, Stochastic uncertainty of advected curves in finite-time unsteady flows, Phys. Rev. E 95 (2017) 062201.

[41] S. Balasuriya, N. Ouellette, I. Rypina, Generalized Lagrangian coherent structures, Phys. D (2018) in press.

[42] A. Hadjighasem, M. Farazmand, D. Blazevski, G. Froyland, G. Haller, A critical comparison of lagrangian methods for coherent structure detection, Chaos 27 (2017) 053104.

[43] R. Pierrehumbert, H. Yang, Global chaotic mixing in isentropic surfaces, J. Atmospheric Sci. 50 (1993) 2462–2480.

[44] G. Voth, G. Haller, J. Gollub, Experimental measurements of stretching fields in fluid mixing, Phys. Rev. Lett. 88 (2002) 254501.

[45] S. Shadden, F. Lekien, J. Marsden, Definition and properties of Lagrangian coherent structures from finite-time Lyapunov exponents in two-dimensional aperiodic flows, Phys. D 212 (2005) 271–304.

[46] P. Tallapragada, S. Ross, A set oriented definition of finite-time Lyapunov exponents and coherent sets, Commun. Nonlin. Sci. Numer. Simu. 18 (2013) 1106–1126.

[47] K. McIlhany, S. Wiggins, Eulerian indicators under continuously varying conditions, Phys. Fluids 24 (2012) 073601.

[48] S. Brunton, C. Rowley, Fast computation of finite-time Lyapunov exponent fields for unsteady flows, Chaos 20 (2010) 017503.

[49] D. Lipinski, K. Mohseni, A ridge tracking algorithm and error estimate for efficient computation of Lagrangian coherent structures, Chaos 20 (2010) 017504.

[50] S. Balasuriya, R. Kalampattel, N. Ouellette, Hyperbolic neighborhoods as organizers of finite-time exponential stretching, J. Fluid Mech. 807 (2016) 509–545.

[51] G. Haller, A variational theory for Lagrangian Coherent Structures, Phys. D 240 (2011) 574–598.

[52] G. Haller, F. Beron-Vera, Geodesic theory for transport barriers in two-dimensional flows, Phys. D 241 (2012) 1680–1702.

[53] M. Farazmand, G. Haller, Computing Lagrangian Coherent Structures from variational LCS theory, Chaos 22 (2012) 013128.

[54] K. Onu, F. Huhn, G. Haller, LCS Tool: an algorithmic introduction to Lagrangian Coherent Structures, J. Comp. Sci. 7 (2015) 26–36.

[55] D. Blazevski, G. Haller, Hyperbolic and elliptic transport barriers in three-dimensional unsteady flows, Phys. D 273–274 (2014) 46–64.

[56] H. Teramoto, G. Haller, T. Komatsuzaki, Detecting invariant manifolds as stationary LCSs in autonomous dynamical systems, Chaos 23 (2013) 043107.

[57] G. Froyland, K. Padberg, Almost invariant sets and invariant manifolds: connecting probablistic and geometric descriptions of coherent structures in flows, Phys. D 238 (2009) 1507–1523.

[58] G. Froyland, S. Lloyd, N. Santitissadeekorn, Coherent sets for nonautonomous dynamical systems, Physica D 239 (2010) 1527–1541.

[59] G. Froyland, N. Santitissadeekorn, A. Monahan, Transport in time-dependent dynamical systems: finite-time coherent sets, Chaos 20 (2010) 043116.

[60] G. Froyland, An analytic framework for identifying finite-time coherent sets in time-dependent dynamical systems, Phys. D 250 (2013) 1–19.

[61] T. Ma, E. Bollt, Relatively coherent sets as a hierarchical partition method, Intern. J. Bifurc. Chaos 23 (2013) 1330026.

[62] G. Haller, A. Hadjighasem, M. Farazmand, F. Huhn, Defining coherent vortices objectively from the vorticity, J. Fluid Mech. 795 (2016) 136–173.

[63] J. Lilly, R. Scott, S. Olhede, Extractig waves and vortices from lagrangian trajectories, Geophys. Res. Lett. 38 (2011) L23605.

[64] E. Bollt, L. Billings, I. Schwartz, A manifold independent approach to understanding transport in stochastic dynamical systems, Physica D 173 (2002) 153–177.

[65] G. Froyland, P. Koltai, Estimating long-term behavior of periodically driven flows without trajectory integration, Nonlinearity 30 (2017) 1948–1986.

[66] There are two branches of each manifold, attaching to a from opposite directions. The method we describe here works for either choice of these branches.

[67] Z. Schuss, Singular perturbation methods in stochastic differential equations of mathematical physics, SIAM Rev. 22 (1980) 119–155.

[68] A. J. Roberts, Slow manifold of stochastic or deterministic multiscale differential equations, online solver, http://www.maths.adelaide.edu.au/anthony.roberts/sdesm.html (2012).

[69] P. Briand, B. Delyon, J. Mémin, On the robustness of backward stochastic differential equations, Stochastic Processes and their Applications 97 (2002) 229–253.

[70] B. Oksendal, Stochastic differential equations, 5th Edition, Universitext, Springer-Verlag, Berlin, 1998. doi:10.1007/978-3-662-03620-4.

[71] G. A. Pavliotis, Stochastic processes and applications, Vol. 60 of Texts in Applied Mathematics, Springer, New York, 2014. doi:10.1007/978-1-4939-1323-7.

[72] S. Balasuriya, A tangential displacement theory for locating perturbed saddles and their manifolds, SIAM J. Appl. Dyn. Sys. 10 (2011) 1100–1126.

[73] P. E. Kloeden, E. Platen, H. Schurz, Numerical solution of SDE through computer experiments, Universitext, Springer-Verlag, Berlin, 1994. doi:10.1007/978-3-642-57913-4.

[74] D. J. Higham, An algorithmic introduction to numerical simulation of stochastic differential equations, SIAM Rev. 43 (3) (2001) 525–546. doi:10.1137/S0036144500378302.

[75] P. Lermusiaux, C.-S. Chiu, G. Gawarkiewicz, P. Abbot, A. Robinson, R. Miller, P. haley, W. Leslie, S. Majumdar, A. Pang, F. Lekien, Quantifying uncertainties in ocean predictions, Oceanography 19 (2006) 90–103.

[76] W. Tang, P. Walker, Finite-time statistics of scalar diffusion in Lagrangian coherent structures, Phys. Rev. E 86 (2012) 045201.

[77] H. Guo, W. He, T. Peterka, H.-W. Shen, S. Collis, J. Helmus, Finite-time Lyapunov exponents and Lagrangian coherent structures in uncertain unsteady flows, IEEE Trans. Visualization Graphics 22 (2016) 1672–2626.

[78] W. Tang, C. Luna, dependence of advection-diffusion-reaction on flow coherent structures, Phys. Fluids 25 (2013) 106602.

[79] M. Engel, J. Lamb, M. Rasmussen, Conditioned Lyapunov exponents for random dynamical systems, arXiv:1805.07177 (2018).

[80] P. Berloff, I. Kamankovich, On spectral analysis of mesoscale eddies. part II: nonlinear analysis, J. Phys. Oceanography 43 (2013) 2528–2544.

[81] K. Stewart, P. Spence, S. Waterman, J. L. Sommer, J.-M. Moines, J. Lilly, M. England, Anisotropy of eddy variability in the global ocean, Ocean Modelling 95 (2015) 53–65.

[82] E. van Sebille, S. Waterman, A. Barthel, R. Punpkin, S. Keating, C. Fogwill, C. Turney, Pairwise surface drifter separation in the western Pacific section of the Southen Ocean, J. Geophys. Res. Oceans 120 (2015) 6769–6781.

[83] J. Lilly, A. Sykulski, J. Early, S. Olhede, Fractional Brownian motion, the Matérn process, and stochastic modeling of turbulent dispersion, Nonlin. Proc. Geophys. 24 (2017) 481–514.